



# 3D hierarchical nanostructures of iron oxides coatings prepared by pulsed laser deposition for photocatalytic water purification



Raju Edla <sup>a,\*</sup>, Andrea Tonezzer <sup>a</sup>, Michele Orlandi <sup>a</sup>, Nainesh Patel <sup>b,\*</sup>, Rohan Fernandes <sup>b</sup>, Nicola Bazzanella <sup>a</sup>, Kalyani Date <sup>b</sup>, D.C. Kothari <sup>b</sup>, Antonio Miotello <sup>a</sup>

<sup>a</sup> Dipartimento di Fisica, Università degli Studi di Trento, I-38123, Povo, Trento, Italy

<sup>b</sup> Department of Physics and National Centre for Nanosciences & Nanotechnology, University of Mumbai, Vidyawagari, Santacruz (E), Mumbai 400098, India

## ARTICLE INFO

### Article history:

Received 9 May 2017

Received in revised form 30 June 2017

Accepted 23 July 2017

Available online 24 July 2017

### Keywords:

Photocatalysis

Pulsed laser deposition

Hematite

Photo-Fenton

Hierarchical nanostructures

## ABSTRACT

3D hierarchical nanostructured hematite ( $\alpha$ -Fe<sub>2</sub>O<sub>3</sub>) coatings containing various shapes were developed by pulsed laser deposition (PLD). A cold pressed, homogeneous mixture of Fe and H<sub>3</sub>BO<sub>3</sub> (Fe + H<sub>3</sub>BO<sub>3</sub>) was used as a target in PLD to deposit the coatings in O<sub>2</sub> atmosphere. Phase explosion phenomenon provided by laser ablation on the target, allowed to form rough, porous and embedded metallic Fe particulates coating with H<sub>3</sub>BO<sub>3</sub> as background on a glass substrate. Subsequent thermal annealing of the as deposited Fe + H<sub>3</sub>BO<sub>3</sub> coating at 600 °C, led to formation of crystalline, hierarchical 3D nanostructured features with nanowires, nanorods, and nanosheets grown from the spherical particulates. Characterization by XRD, Micro-Raman, XPS, SEM and KPM analysis provided information on the systematic phase and morphology transformation from metallic Fe to hierarchical Iron oxide. Stress-induced phase segregation and stress release process during thermal annealing are suggested as the growth mechanism for the nanostructures. Photocatalytic activity measurements were studied with the coating in presence of Methylene Blue dye through Photo-Fenton process. To understand the effect of precursors, morphology, and synthesis technique (physical and chemical), similar hematite nanostructures were also prepared by thermal annealing of as deposited metallic Fe coating, hematite nanoparticles assembled coating by PLD, and by hydrothermal chemical method respectively. All these coatings showed less photocatalytic activity as compared to the hematite coating obtained from thermal annealing of Fe + H<sub>3</sub>BO<sub>3</sub> sample. A series of various parameters such as effect of H<sub>2</sub>O<sub>2</sub> concentration, effect of pH, water medium and recyclability tests for 10 times were performed, and all revealed promising results in terms of enhanced activity and high mechanical stability of the coatings. Presence of various 3D hierarchical nanostructures, high aspect ratio, more exposed active sites, increased interactions between catalyst surface and reactant dye molecules, and enhanced charge carrier separation, with immobilized stable coating form developed by PLD contributed to achieve the enhanced and stable photocatalytic activity.

© 2017 Elsevier B.V. All rights reserved.

## 1. Introduction

The significant issues facing today, are the environmental issues especially of air and water pollution caused by human activities [1–3]. Presence of organic pollutants in wastewater is a matter of great concern mainly due to the related health issues and level of damage caused to the aquatic life [4]. The current purification technologies are not efficient to completely remove the organic pollutants miscible in water, in addition they produce secondary

pollutants which require further treatment thus increasing the cost of the process [5]. Advanced oxidation process (AOP) such as Photo-Fenton reaction is a cost effective and efficient process to remove organic pollutant in presence of H<sub>2</sub>O<sub>2</sub> and metal cations [6,7]. More importantly photo-Fenton reaction may proceed by absorption of visible light which is a big advantage over other AOP such as direct photolysis of H<sub>2</sub>O<sub>2</sub> and photoexcitation of TiO<sub>2</sub> requiring high intensity UV light [8].

Homogeneous route of Fenton reaction involving metal cations produces large amount of sludge residue which need to be separated. Therefore, the heterogeneous transition metal oxide has attracted a lot of attention to generate hydroxyl radicals by Photo-Fenton reaction under light [9]. For this application, Hematite ( $\alpha$ -Fe<sub>2</sub>O<sub>3</sub>) is one of the most promising photocatalyst owing to its

\* Corresponding authors.

E-mail addresses: [raju.edla@gmail.com](mailto:raju.edla@gmail.com) (R. Edla), [\(N. Patel\).](mailto:nainesh11@gmail.com)

high thermodynamic stability, being in addition low-cost, abundant, and non-toxic nature [10]. Having a band gap of 2.2 eV also assists in absorbing visible light with high absorption coefficient. Thereby, posing a great interest in this material for solar photo assisted applications, especially for degradation of organic pollutants in industrial wastewater.  $\alpha$ -Fe<sub>2</sub>O<sub>3</sub> has remarkable applications in Li ion batteries [11–15], magnetic materials [16,17], photo assisted solar water splitting [18–22], sensors [23–26], and cancer treatment [27,28]. To achieve high efficiency in these applications, efficient transport of the generated charge carriers towards the surface is highly needed. In addition to this feature, high surface area with large number of active sites having favorable catalytic kinetics is also desirable. Various morphological nanostructures such as porous, nanowires, nanorods, nanoflakes, nanosheets and 3D- urchin like solid and hollow iron oxides were adapted to increase the surface reactivity [17,29–33]. Along with nanostructures of the iron oxide, the oxide phase (hematite, magnetite-Fe<sub>3</sub>O<sub>4</sub>) with corresponding oxidation states (Fe<sup>+2</sup> and Fe<sup>+3</sup>) critically alters the photocatalytic properties. So, it's very important to control these parameters in achieving a desirable photocatalytic activity.

Several morphological strategies were reported to improve the photocatalytic water treatment by iron oxides. Shape controlled  $\alpha$ -Fe<sub>2</sub>O<sub>3</sub> for phenol and 4-Chlorophenol degradation [34,35], 1D nanoparticles form for Rhodamine Dye-B degradation [31], supported on activated carbon fiber for Acid red B degradation [36], different exposed surface facets [37] and nano urchins for Congo Red dye degradation [38], 3D SnO<sub>2</sub>/ $\alpha$ -Fe<sub>2</sub>O<sub>3</sub> semiconductor hierarchical nano-heterostructures [39], Fe<sub>2</sub>O<sub>3</sub>/TiO<sub>2</sub> nanoparticles [40] and phase controlled iron oxide [41] for Methylene Blue (MB) dye degradation were studied in presence of Photo-Fenton reaction. Also, other strategies such as plasmonic (metal semiconductor composite), heterostructures and various forms of Fe based photo-Fenton catalysts were reported for degradation of MB dye, Rhodamine dye and other organic dyes [42–46]. However, most of the reported  $\alpha$ -Fe<sub>2</sub>O<sub>3</sub> catalyst for removal of organic pollutant by Photo-Fenton reaction is in powder form, where recovering and recycling are the major issues. Along with these problems, the inherent magnetic nature allows the  $\alpha$ - Fe<sub>2</sub>O<sub>3</sub> catalyst particles to aggregate very fast in the wastewater and the stability of the catalyst is hindered [41,47,48]. This drawback restricts the powder catalyst to be utilized for continuous flow water treatment reactor. Immobilization of the photocatalyst (IPC) as coatings on a substrate support could be an appropriate solution to avoid these problems. Immobilizing Co<sub>3</sub>O<sub>4</sub> nanostructured coatings on glass substrates showed an excellent improvement over unsupported catalyst NPs in terms of both catalyst stability and activity [49–53]. Though IPC can be synthesized with several physical and chemical methods [54–57], however establishing nanostructures as coating surface with desired morphology and size is still a difficult task to achieve. PLD is a state of art technique for producing several nanostructures from 0D nanoparticles, 1D nanowires, 2D nanosheets to 3D porous and hierarchical nanostructures [49,52,53]. Several deposition parameters in PLD can be tuned to realize required morphology of any dimensions [58].

Here we address a novel synthesis of 3D hierarchical Iron oxide (hematite) nanostructures as an IPC by thermal annealing of Fe + H<sub>3</sub>BO<sub>3</sub> particulates coating deposited by PLD. The nanostructures were deposited on glass substrates and characterized with structural and morphological techniques. Photocatalytic degradation of MB dye, as a model pollutant, was performed using this coating by Photo-Fenton reaction. The enhanced photocatalytic activity and the possible mechanism for the nanostructures growth are explained with the support of the characterization techniques. The stability and reusability of these nanostructures were also

investigated in various conditions to verify the possible viability of these coatings for industrial applications.

## 2. Experimental

### 2.1. Pulsed laser deposition of iron oxide coatings

Mixture of metallic Fe and H<sub>3</sub>BO<sub>3</sub> (Fe + H<sub>3</sub>BO<sub>3</sub>) powders was first prepared and then compressed in form of a circular disk to realize the target for synthesizing iron oxide 3D urchin-like coatings by PLD using a KrF excimer laser (Lambda Physik) with an operating wavelength at 248 nm, pulse duration of 25 ns, and repetition rate of 20 Hz. The fluence of laser was always maintained at 3 J/cm<sup>2</sup> for ablation. Details of the PLD deposition apparatus and mechanisms involved in the laser ablation process have been presented in our past reports [51,59]. The PLD chamber was evacuated up to a base pressure of 10<sup>-6</sup> mbar prior to all the depositions and later, during deposition, the O<sub>2</sub> pressure was maintained at 1.5 × 10<sup>-2</sup> mbar for the Fe + H<sub>3</sub>BO<sub>3</sub> coating. The coatings were deposited on Si and glass substrates by maintaining the target to substrate distance at 4.5 cm, with substrate position parallel to the target, or normal to the flow velocity of the plume expansion. The deposition of metallic Fe films was carried out in vacuum, as well as in reactive O<sub>2</sub> atmosphere (pressure of 4.5 × 10<sup>-2</sup> mbar) at room temperature. Thermal treatment of all the deposited coatings was carried out in air at temperatures of 400, 500 or 600 °C for 4 h with a heating rate of 5 °C/min in order to grow the hierarchical urchin-like structures.

### 2.2. Hydrothermal method to synthesize 3D flower-like structures

All the chemicals were obtained from Sigma Aldrich and used as received. Iron oxide flower-like structures were prepared by hydrothermal synthesis [60]. 0.76 mmol of (NH<sub>4</sub>)<sub>2</sub>SO<sub>4</sub>, 15 mmol of FeCl<sub>3</sub> · 6H<sub>2</sub>O were dissolved in 30 ml of deionized H<sub>2</sub>O and sealed in a custom-made Teflon-lined aluminum autoclave with a capacity of 50 ml. Si and glass substrates were placed in the autoclave to obtain coatings. The reactor was heated at 120 °C for 12 h and was naturally cooled down to reach room temperature. After that a red precipitate coating on the substrates was collected and washed several times with water and ethanol, and dried in air at 80 °C for 1 h. The remaining powder was recovered by filtering with a sintered glass Buchner funnel and washed with water and ethanol. Thermal treatment was carried at 600 °C in air for 2 h with a heating rate of 5 °C min<sup>-1</sup> to obtain the urchin-like structures.

### 2.3. Characterization

The surface morphology of all the coatings prepared with PLD and the chemically obtained samples was examined using scanning electron microscope (SEM-FEG, JSM 7001F, JEOL) equipped with energy-dispersive spectroscopy analysis (EDS, INCA PentaFET-x3). Micro-Raman analysis was performed using an HORIBA JobinYvon Lab RAM Aramis Raman spectrometer with diode pumped solid state laser operating at 634 nm. The signal was collected on an air-cooled multichannel CCD, with a wavenumber accuracy of ±1 cm<sup>-1</sup> in the range of 200–1500 nm. Structural characterization was carried out by X-Ray Diffractometer (XRD) using the Cu K<sub>α</sub> radiation ( $\lambda = 1.5414 \text{ \AA}$ ) in Bragg-Brentano ( $\theta$ -2 $\theta$ ) configuration. Absorption spectra were obtained using a VARIAN Cary 5000 UV-vis-NIR spectrophotometer. The surface composition and chemical states of each element in the samples were examined by X-ray photoelectron spectra (XPS) using a PHI 5000 Versa Probe II instrument equipped with a monochromatic Al K<sub>α</sub> (1486.6 eV) X-ray source and a hemispherical analyzer. Appropriate electrical charge compensation was employed to perform the analysis and binding energy was

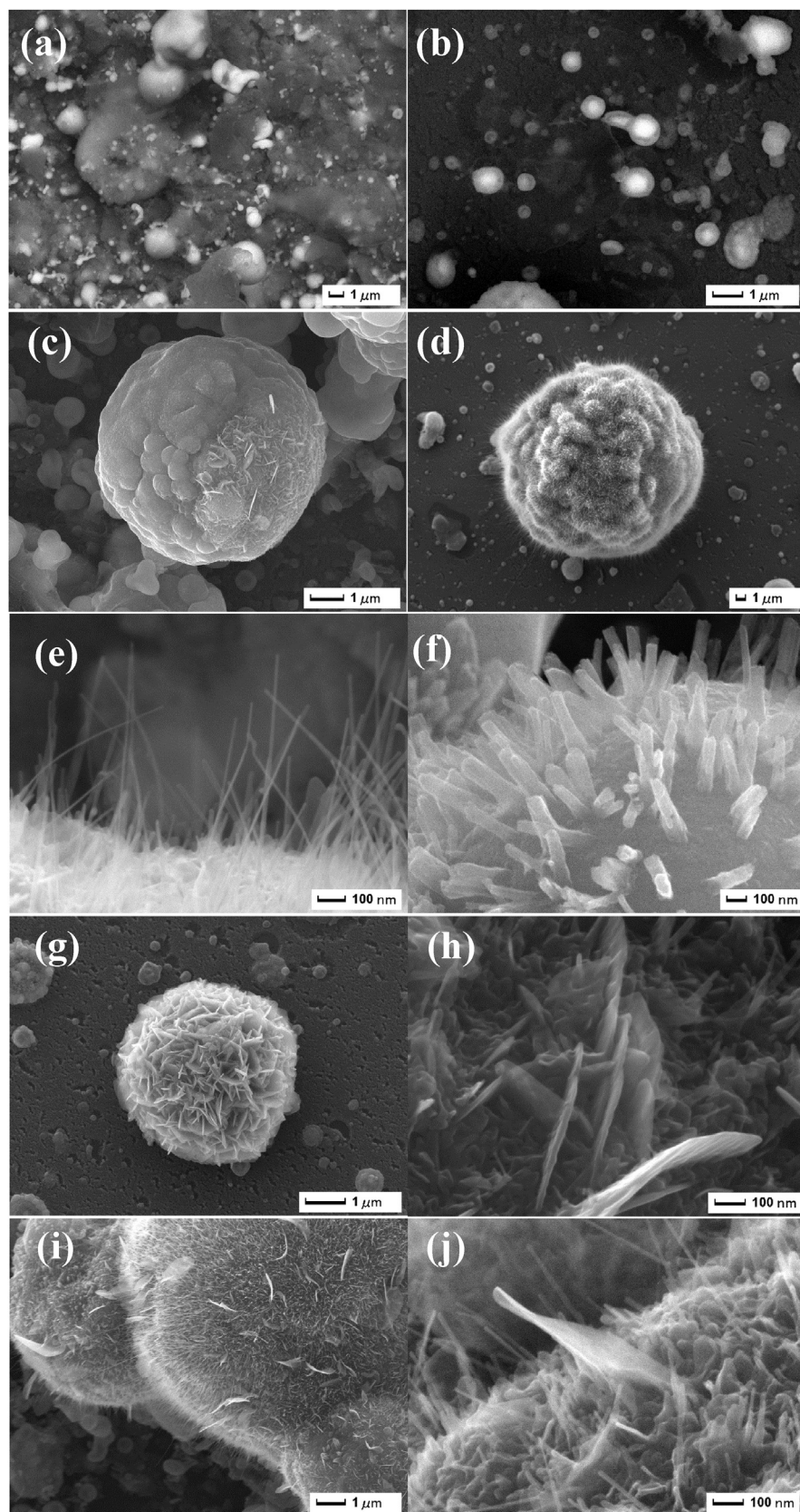


**Fig. 1.** SEM images of Fe-H<sub>3</sub>BO<sub>3</sub> coating synthesized by PLD (a) As deposited and annealed in air for 4 h at (b) 400 °C, (c) 500 °C and (d)–(j) 600 °C.

referenced to the C 1s peak. Kelvin Probe Microscope (KPM) imaging was performed in air using Bruker Nanoscope equipped with a 100  $\mu\text{m}$  scanner. Commercial Antimony doped Si cantilever coated

with platinum from Bruker (SCM-PIT) with an elastic modulus of  $\sim 2.5 \text{ N m}^{-1}$  was used. The surface potential measurements were performed by applying 2 V ac bias to the tip to produce an electric

force on the cantilever which is proportional to CPD between tip and sample.

#### 2.4. Photocatalytic measurements

The photocatalytic performance was evaluated by studying the degradation of MB dye as a model pollutant. 30 ml of 10 ppm MB (Alfa Aesar) dye solution mixed with hydrogen peroxide ( $H_2O_2$ ), as an oxidizing agent, were used for degradation by Photo-Fenton reaction. The catalyst coatings (prepared on glass slide of area  $2.5 \times 7.5$  cm) were dipped in the above prepared MB dye solution and kept in dark under stirring at 300 rpm for 30 min to establish adsorption equilibrium between the solution and the catalyst surface. The weight of the catalyst was maintained approximately 2 mg during each photocatalytic reaction such that it covers the entire surface of the glass slide. A tungsten lamp (225 W) emitting visible light spectrum was used as the light source. 1 ml of MB dye solution was collected after established time intervals during the reaction to study the amount of degradation by measuring the UV-vis absorption spectra and analyzing the characteristic peak at 664 nm, of MB dye. All the photocatalysis experiments were performed at room temperatures; and effects of using different  $H_2O_2$  concentration and pH values were investigated. Reusability of the urchin-like structure was evaluated by collecting the coating after each degradation reaction, washing it with distilled water and reintroducing it into the dye solution for another run; sample was recycled up to 10 times in a similar manner.

### 3. Results and discussion

Fig. 1 presents the SEM image of Fe +  $H_3BO_3$  coatings deposited by PLD in  $O_2$  atmosphere and treated at three different temperatures  $400^\circ C$ ,  $500^\circ C$ , and  $600^\circ C$  in air. Spherical particulates with size distribution in the range of few nanometers to 2–5 micrometers decorated in a porous-rough matrix are visible on the surface of as deposited (AD) coatings (Fig. 1a). After annealing at  $400^\circ C$  in air, the core-shell structure of the particulates starts to appear clearly where the high contrast between core and shell indicates the presence of different elements in each part (Fig. 1b). The thickness of the shell is around 200–300 nm and seems to be independent of particulates size. Further annealing at  $500^\circ C$  causes disintegration of the shell forming cracks or porous protrusions with the formation of small particles on the surface of the particulates (Fig. 1c). Coatings annealed at  $600^\circ C$  in air for 4 h show a morphological transformation from spherical particulates to an urchin-like structure with evolution of nanowires (NWs) vertical to the surface of the particulates (Fig. 1d). NWs, having diameter in range of 8–10 nm and length about 500–600 nm, acquire high aspect ratio (Fig. 1e). Surface coverage density of these NWs in urchin-like particles is very high of about  $(4.2 \pm 0.2) \times 10^{14}$  NWs/m<sup>2</sup>. Along with NWs, certain particulates also display the presence of nanorods (NRs) with width of 70–80 nm and length of 200–250 nm (Fig. 1f). Some particulates are also observed having flower-like structures (Fig. 1g) formed with nano-sheets (NSs) of thickness 15–20 nm and width of 500–600 nm (Fig. 1h). This forms a porous hierarchical structure possessing high surface area. Besides particulates having individual structure (NWs, NRs, or NSs) the combination of two (Fig. 1i) or all three nanostructures are also visible in few particulates (Fig. 1j). The formation mechanism of the nanostructures is proposed in the later section.

XRD measurements were performed on the coatings of the Fe- $H_3BO_3$  annealed at various temperatures, to identify the presence of crystal structure and shown in Fig. 2a. The AD coating (Fig. 2a) shows only the presence of metallic Fe (JCPDS No. 06-0696) [16,61,62] and  $H_3BO_3$  (JCPDS card No. 73-2158) [63] peaks which

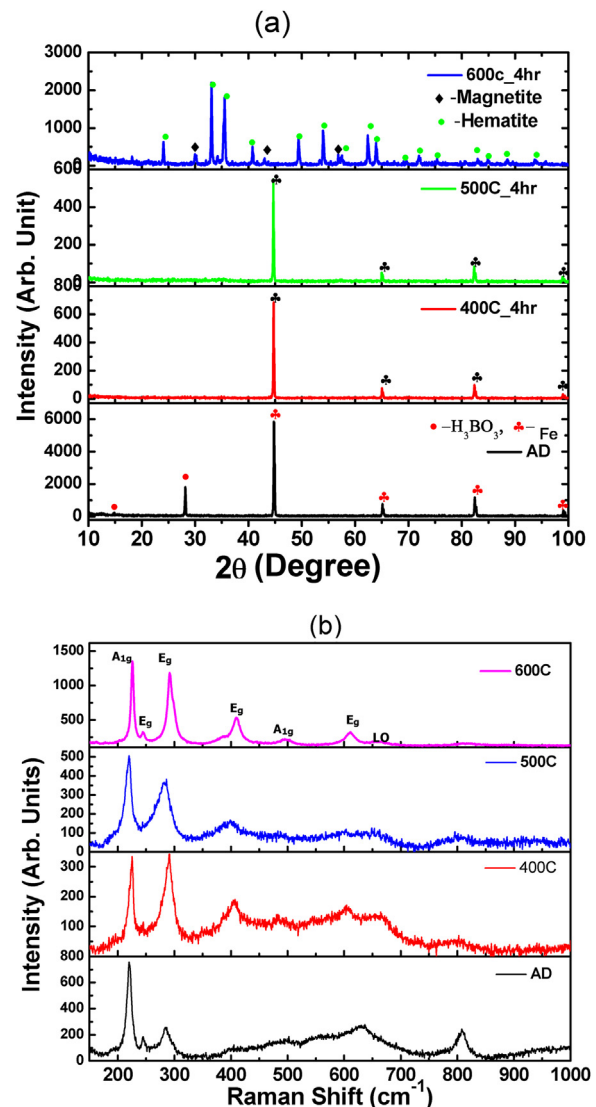


Fig. 2. (a) XRD pattern and (b) Raman spectra of Fe- $H_3BO_3$  coating synthesized by PLD, as deposited and annealed in air for 4 h at  $400^\circ C$ ,  $500^\circ C$  and  $600^\circ C$ .

are very sharp and intense. No other phases were detected thus maintaining the composition of the PLD target in the coating. The annealed coatings at  $400$  and  $500^\circ C$  revealed only presence of the Fe metallic phase with sharp peaks and exhibited complete disappearance of  $H_3BO_3$  phase, which was expected as  $H_3BO_3$  melts at  $171^\circ C$  and decomposes above  $350^\circ C$ . However, annealing at  $400^\circ C$  and  $500^\circ C$  for 4 h does not demonstrate any signs of oxidation of the Fe particles. The peaks due to Fe oxides appear upon heat treatment at  $600^\circ C$ , with majority of the oxide is in the form of  $\alpha$ - $Fe_2O_3$  and with small amount of magnetite ( $Fe_3O_4$ ). Since the magnetite phase transforms to hematite above  $200^\circ C$  in air, we believe that the observed magnetite must be present in the core of the particulates where a limited presence of oxygen may allow only partial oxidation to form the hematite phase.

Micro-Raman spectra were acquired in order to investigate the existence of Fe oxide phase and are presented in Fig. 2b. AD and the coatings treated at  $400^\circ C$  and  $500^\circ C$  displayed two main peaks centered at  $220$  and  $280\text{ cm}^{-1}$  mainly assigned to  $A_{1g}$  and  $E_g$  vibration in hematite structure [64]. The small peak at  $405\text{ cm}^{-1}$  only present in coating annealed at  $400^\circ C$  and  $500^\circ C$ , is also attributed to hematite nanostructure. The broad nature of these three peaks also indicates partial oxidation of the coat-

ings. The peak at  $807\text{ cm}^{-1}$  in AD coating indicates the presence of boron oxide ( $\text{B}_2\text{O}_3$ ) on the surface [65], while no sign of  $\text{H}_3\text{BO}_3$  (peak at  $880\text{ cm}^{-1}$ ) [66]. The strong Raman scattering peaks at  $280$  and  $401\text{ cm}^{-1}$  is also pertinent to  $\text{FeBO}_3$  phase [67] thus we cannot neglect the presence of this phase on the surface. The coating annealed at  $600^\circ\text{C}$  (Fig. 2b) generates fully developed hematite crystalline phase as evident by the increased intensity and sharpness of the peaks. The typical Raman bands of a hematite phase at ( $\text{A}_{1g}$ ) $226\text{ cm}^{-1}$ , ( $\text{E}_g$ ) $245\text{ cm}^{-1}$ , ( $\text{E}_g$ ) $292\text{ cm}^{-1}$ , ( $\text{E}_g$ ) $411\text{ cm}^{-1}$ , ( $\text{A}_{1g}$ ) $497\text{ cm}^{-1}$ , ( $\text{E}_g$ ) $612\text{ cm}^{-1}$ , ( $\text{LO}$ ) $661\text{ cm}^{-1}$  and phonon-phonon scattering at  $1320\text{ cm}^{-1}$  are observed [64,68]. The absence of Raman scattering modes at  $313$ ,  $540$ , and  $669\text{ cm}^{-1}$  due to the magnetite phase, suggests that only hematite is present on the coatings surface after morphological transformation at  $600^\circ\text{C}$  heat treatment [64]. Ideally the differentiation of both hematite and magnetite phases on the surface through Raman spectroscopy is difficult due to the dominating signal produced by hematite in comparison to magnetite. Thus, in order to further verify the chemical states of Fe on the surface of nanostructures, XPS measurement was performed.

Along with residual carbon, only Fe, O and B elements are detected in the elemental survey scan of XPS. In Fe 2p XPS spectra (Fig. 3a), two broad peaks assigned to  $2\text{p}_{3/2}$  and  $2\text{p}_{1/2}$  levels are observed for all the four coatings. However, the de-convolution of these peaks shows that in AD coatings Fe is in form of  $\text{Fe}^{3+}$  state in  $\text{FeOOH}$  (as observed at  $712\text{ eV}$  for  $2\text{p}_{3/2}$  state) and a corresponding satellite peak is observed at higher BE [69]. Surface oxidation in the ambient condition is the mainly responsible for this chemical species. In the case of the coatings annealed at  $400^\circ\text{C}$  and  $500^\circ\text{C}$ , the  $2\text{p}_{3/2}$  peak is de-convoluted into two peaks centered at  $710.5\text{ eV}$  and  $711.4\text{ eV}$  assigned to  $\text{Fe}^{3+}$  state in  $\alpha\text{-Fe}_2\text{O}_3$  and  $\text{FeBO}_3$  respectively and their corresponding satellite is seen at  $719\text{ eV}$  and  $714.5\text{ eV}$  respectively [70]. Nevertheless, the amount of  $\text{FeBO}_3$  is higher than  $\alpha\text{-Fe}_2\text{O}_3$  for  $400^\circ\text{C}$  treated coating, while both the phases are present in equal amount at  $500^\circ\text{C}$ . At highest temperature treatment ( $600^\circ\text{C}$ ), the peak due to  $\alpha\text{-Fe}_2\text{O}_3$  ( $710.4\text{ eV}$ ) dominates significantly over  $\text{FeBO}_3$  ( $711.4\text{ eV}$ ) thus indicating the formation of  $\alpha\text{-Fe}_2\text{O}_3$  phase as confirmed by XRD and Raman analysis. Similar characteristics are also observed in  $\text{Fe}_{2\text{p}1/2}$  level. B 1s XPS spectra shown in Fig. 3b display one peak for all the samples, but the deconvolution results in two peaks for the as deposited (AD) and  $600^\circ\text{C}$  annealed samples (Fig. 3b). For AD the de-convoluted peaks at  $192.5\text{ eV}$  (56%) and  $193.3\text{ eV}$  (44%) are attributed to boron oxide ( $\text{B}_2\text{O}_3$ ) and  $\text{H}_3\text{BO}_3$  respectively, thus confirming the Raman and XRD results showing the presence of  $\text{B}_2\text{O}_3$  and  $\text{H}_3\text{BO}_3$  respectively. Single peak centered at  $191.7\text{ eV}$  assigned to  $\text{FeBO}_3$  is observed for  $400^\circ\text{C}$  and  $500^\circ\text{C}$  treated coatings. For the sample annealed at  $600^\circ\text{C}$  the majority (80%) of  $\text{H}_3\text{BO}_3$  is transformed into  $\text{B}_2\text{O}_3$  displaying a peak at  $192.6\text{ eV}$  in the B 1s XPS spectra. O 1s XPS spectra are shown in Fig. 3c, with de-convoluted peaks for the annealed samples (Fig. 3c). For AD coating, the O 1s XPS spectrum displays a single peak at  $532.4\text{ eV}$  indicating the possible presence of  $\text{FeOOH}$ ,  $\text{B}_2\text{O}_3$  and  $\text{H}_3\text{BO}_3$  species in the sample. On the other hand, for heat treated samples the deconvolution of O 1s state displays the peaks due to oxygen in  $\alpha\text{-Fe}_2\text{O}_3$  ( $530.1\text{ eV}$ ) and  $\text{FeBO}_3$  ( $531.5\text{ eV}$ ). Additional peak at  $532.4\text{ eV}$  due to  $\text{B}_2\text{O}_3$  is only visible in  $500^\circ\text{C}$  and  $600^\circ\text{C}$  treated samples with higher intensity in the later case. Thus from the XPS analysis it is clear that after the deposition the sample surface is composed of  $\text{H}_3\text{BO}_3$ ,  $\text{B}_2\text{O}_3$  and  $\text{FeOOH}$  which transforms to mainly  $\text{FeBO}_3$  and some  $\alpha\text{-Fe}_2\text{O}_3$  after annealing upto  $500^\circ\text{C}$ . Later at  $600^\circ\text{C}$  most of the  $\text{FeBO}_3$  disintegrates to form crystalline  $\alpha\text{-Fe}_2\text{O}_3$  and amorphous  $\text{B}_2\text{O}_3$  on the surface.

It is very difficult to detect the surface stress by XRD because only small amount of signal is contributed from the surface in XRD pattern. Kelvin probe Microscope (KPM) is used to measure the surface potential of the coatings, which is related to the surface

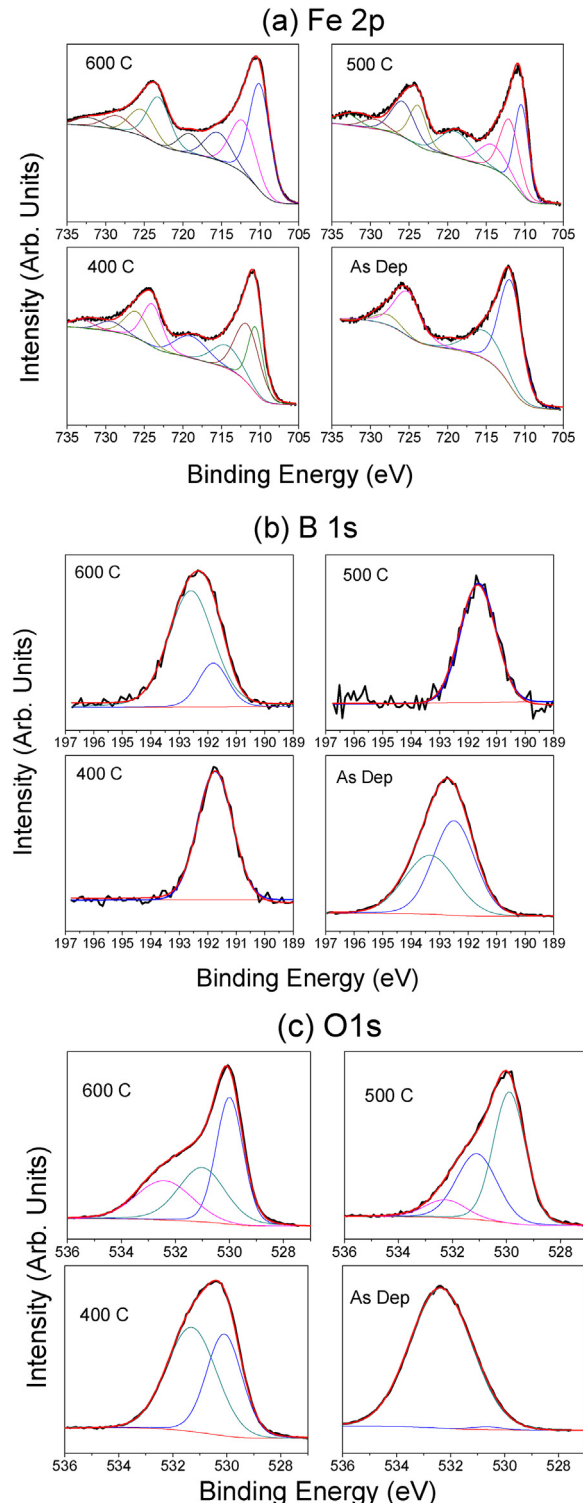


**Fig. 3.** XPS spectra of  $\text{Fe-H}_3\text{BO}_3$  coating synthesized by PLD, as deposited and annealed in air for  $4\text{ h}$  at  $400^\circ\text{C}$ ,  $500^\circ\text{C}$  and  $600^\circ\text{C}$  in (a) Fe 2p, (b) B 1s and (c) O1s level.

stress [71,72]. Most importantly, this technique provides information of very small area ( $10 \times 10 \mu\text{m}^2$ ) of the coating. Fig. 4 shows the KPM image with surface potential scale of all the four coatings and corresponding AFM topography are reported in the Supporting information (Fig. S1). The surface potential recorded for as deposited ( $8.54\text{ mV}$ ) coating increases with treatment temperature at  $400^\circ\text{C}$  ( $9.21\text{ mV}$ ) and reaches maximum at  $500^\circ\text{C}$  ( $12.5\text{ mV}$ ).

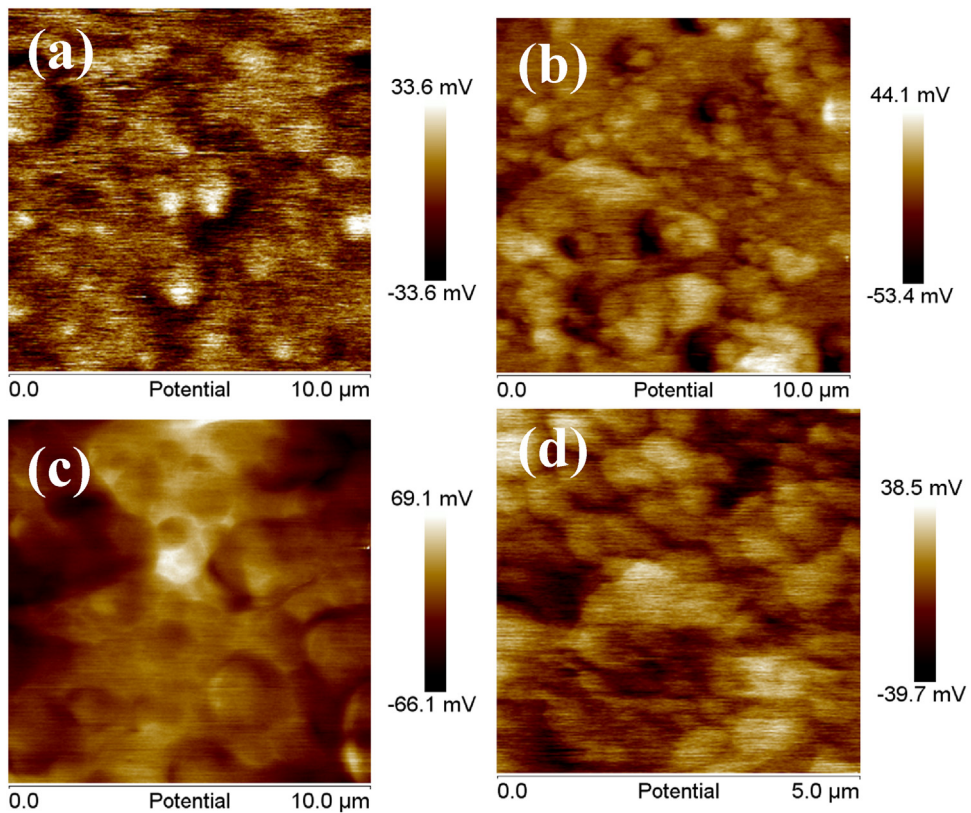


**Fig. 4.** KPM image of Fe-H<sub>3</sub>BO<sub>3</sub> coating synthesized by PLD, (a) as deposited and annealed in air for 4 h at (b) 400 °C, (c) 500 °C and (d) 600 °C.

After annealing at 600 °C the surface potential decreases to a value (8.87 mV) very close to the as deposited coating. Since the surface potential is directly proportional to the stress induced on the surface, it is concluded from the KPM data that the level of stress on the coating increased with the annealing temperature and reached maximum at 500 °C. The release of surface stresses with the heat treatment at 600 °C correlated well with the phase transformation to  $\alpha$ -Fe<sub>2</sub>O<sub>3</sub> phase observed in XRD, XPS and Raman, and nano morphological changes observed in SEM.

### 3.1. Mechanism of nanostructures formation

In most cases 1D nanostructures (NWs and NRs) are grown by vapor–liquid–solid (VLS) or vapor–solid (VS) mechanism involving catalytic tip. For such growth mechanism, the temperature must be maintained higher than the eutectic temperature of the two elements (catalyst and growing element). In present case, the annealing temperatures are far below the eutectic temperature (1165 °C) of Iron–boron alloy and the melting points of Iron (1538 °C), B (2076 °C), Fe<sub>3</sub>O<sub>4</sub> (1597 °C) and Fe<sub>2</sub>O<sub>3</sub> (1565 °C). Thus, VLS and VS mechanisms are ruled out for the growth of the 3D hierarchical nanostructures. Hence the obtained nanostructures with PLD deposited coating and subsequent annealing is mainly attributed to the stress induced growth. Based on the analysis of the SEM, XRD, Raman, XPS and KPM results, we propose a probable mechanism of nanostructure formation as follows.

In AD coating, the presence of particulates of wide range of sizes is due to the phase explosion process occurring when high-energy laser impinges the target. At sufficiently high laser fluence the target material surface reaches a temperature of  $\sim 0.9T_c$  ( $T_c$  is the thermodynamic critical temperature), causing a very high homogeneous nucleation of vapor bubbles. The target surface then makes a rapid transition from superheated liquid to a matrix of vapor and

liquid droplets, which leave the irradiated target surface and get deposited on the substrate [73]. The size and the number density of these particles are related to the laser energy and target properties [51,74]. As confirmed by XRD, AD coating is composed of H<sub>3</sub>BO<sub>3</sub> and Fe, as in the target, where H<sub>3</sub>BO<sub>3</sub> exists in the form of rough background and Fe is in the form of spherical particulates. Nevertheless, micro-Raman and XPS displayed only presence of oxides on the surface. Thereby, from these observations, the probable structure of the spherical particles could be in the form of a core–shell, where the core is made up of Fe metal and the shell contains the oxides of Fe and B. Such core–shell morphology was also observed in PLD deposited coating of Co–B where the core is due to Co metal and the shell is composed of Co–B–O [53]. After annealing at temperature around 400 °C, this core–shell structure is clearly evident in the SEM image as the shell thickness increased because of further oxidation. Crystalline Fe (as indicated in XRD) forms the core and the shell is composed of amorphous FeBO<sub>3</sub> as detected by XPS spectra. The thickness of the shell (200–300 nm) and difference in the thermal expansion coefficient of FeBO<sub>3</sub> ( $1.5 \times 10^{-6}$  K<sup>-1</sup>) and Fe metal ( $12 \times 10^{-6}$  K<sup>-1</sup>) creates increasing stress between the core and the shell with the increase in annealing temperature as confirmed by the surface potential measured by KPM. This stress is maximum after treatment at 500 °C (as concluded from the KPM analysis), leading to the partial disintegration of FeBO<sub>3</sub> phase and the formation of  $\alpha$ -Fe<sub>2</sub>O<sub>3</sub> and B<sub>2</sub>O<sub>3</sub> phases in the shell, as validated by Raman and XPS, with crack and small particles (as seen in SEM images). At 600 °C the resulting stress is released by complete disintegration of FeBO<sub>3</sub> and by the formation of B<sub>2</sub>O<sub>3</sub> and various nanostructures (NWs, NRs and NSs) of  $\alpha$ -Fe<sub>2</sub>O<sub>3</sub>, where cracks formed at 500 °C allow the extrusion of Fe from the core. This phenomenon happens by outward diffusion of metallic element along the nucleation centers of initially formed oxide grains on the surface of large particles at 400 and 500 °C (SEM image at 500 °C in Fig. 1c) that reacts with

gaseous  $O_2$ . This leads to the formation of nanostructures accompanied by the release of stresses. The extrusion marks on the surface of NWs, NRs and NSs also confirm the stress induced growth of nanostructures. In summary, hierarchical structure mainly consists of  $\alpha$ - $Fe_2O_3$  (NWs, NRs or/and NSs) on the surface and the core, which holds these nanostructures, is composed of mainly  $B_2O_3$  and  $\alpha$ - $Fe_2O_3$ . Some  $Fe_3O_4$  (magnetite) remains because of partial oxidation and is present in the interior of the core. However, the final mechanism for the formation of 1D NRs and NWs, and 2D NSs is still not clear from the present experiments and demands further studies.

### 3.2. Photocatalytic measurements

As a model pollutant MB dye was used to study the photocatalytic activity, promoted by the Photo-Fenton reaction, of the hierarchical nanostructures prepared by PLD. Monitoring the variation in absorption peak position of MB dye at 664 nm as function of irradiation time, through optical absorbance measurements, gives knowledge about efficiency of photocatalytic activity of the catalyst. The degradation of the MB dye solution was quantitatively expressed as degradation ratio ( $1 - [C/C_0]$ ), where  $C_0$  is the absorbance at time  $t=0$  and  $C$  is the absorbance taken at a given reaction time. Adsorption phenomenon is the main precondition for any heterogeneous photocatalytic reaction. Hence, all the catalyst coatings were kept in dark with the MB dye solution for 30 min with stirring, to achieve the adsorption-desorption equilibrium between the solution and the catalyst surface.

Degradation of the MB dye was examined in the presence of only light, with  $H_2O_2$  and light, and with only catalyst coating in the presence of light (Supporting information: Fig. S2). In all these combinations, very low amount of degradation was obtained even after prolonged period of 6–8 h. Complete degradation of the dye was observed in presence of catalyst after 120 min, only when exposed to visible light in the presence of  $H_2O_2$  (Fig. 5) as an additional oxidant, thus indicating that the dye is degraded by Photo-Fenton reaction scheme. Further confirmation of this process was obtained by varying the  $H_2O_2$  concentration (Supporting information: Fig. S3) and found that degradation rate increases with  $H_2O_2$  concentration and attains saturation at 1 M  $H_2O_2$ . These results are compatible with Fenton reaction where degradation mechanism proceeds with the formation of hydroxyl radicals and oxidant concentration is directly proportional to the number of hydroxyl radicals generated [7]. Thus increasing the  $H_2O_2$  concentration enhances the degradation rate.

The degradation of MB dye by Photo-Fenton reaction was studied using the present coatings annealed at different temperatures to investigate the effect of hierarchical nanostructures on photocatalyst activity (Fig. 5). The coatings annealed at 400 °C and 500 °C were able to degrade only 65% and 84% of MB dye in 240 min. On

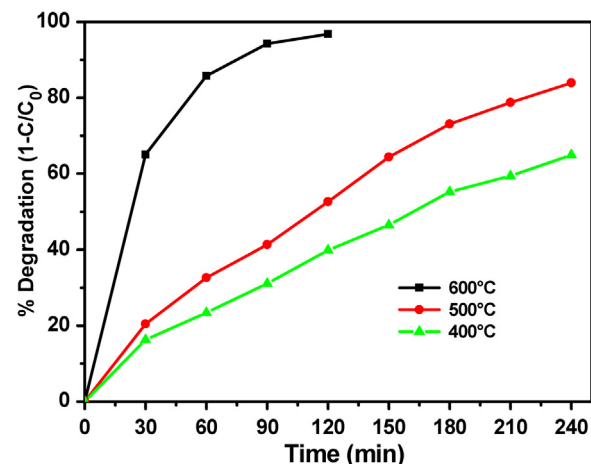


**Fig. 5.** Time dependent photocatalytic degradation ratio of MB solution in presence of  $H_2O_2$  and visible light using  $Fe-H_3BO_3$  coatings synthesized by PLD and annealed in air for 4 h at 400 °C, 500 °C and 600 °C.

the other hand, the coating treated at 600 °C with hierarchical nanostructures produced 100% degradation in just 120 min, thus proving that urchin-like and flower-like nanostructures with crystalline  $\alpha$ - $Fe_2O_3$  structures are highly active for the Photo-Fenton reaction. However, it is not clear how much is the contribution from a) urchin like, b) flower-like, or c) crystalline  $\alpha$ - $Fe_2O_3$  phases. To further shed light, we have prepared three different coatings with: a) only nanoparticles of crystalline  $\alpha$ - $Fe_2O_3$ , b) only urchin-like structure with crystalline NWs of  $\alpha$ - $Fe_2O_3$  and c) only flower-like nanostructures with crystalline 2D nanosheets of  $\alpha$ - $Fe_2O_3$  and designated as coating A, B and C respectively. NPs assembled coating was synthesized by the method reported in our previous work by Orlandi et al. [75], by using PLD. To obtain coating B, the pure Fe film was deposited by PLD in vacuum with particulates of Fe having size in wide range of few nanometers and 2–5 micrometers as observed for  $Fe + H_3BO_3$  coating. Finally, the flower-like nanostructure on the coating C was synthesized by chemical hydrothermal method. All these coatings were heat treated in air at 600 °C to obtain crystalline  $\alpha$ - $Fe_2O_3$  phase on the surface and, for coating B, to induce nanostructures formation. The SEM images of coatings B and C are presented in Fig. 6 while SEM image of coating A is reported in our previous work [75]. The compact coating of  $\alpha$ - $Fe_2O_3$  prepared by PLD showed NPs having size in a narrow range of 10–20 nm densely arranged on the surface [75]. Pure Fe film deposited by PLD in vacuum and annealed in air at 600 °C displayed only urchin-like structure on the surface with NWs supported on core (Fig. 6a). The diameter (10–15 nm) and length (1–2  $\mu$ m) of NWs are comparable to those obtained in  $Fe + H_3BO_3$  coatings. The coating prepared by hydrothermal method showed flower-like morphology formed

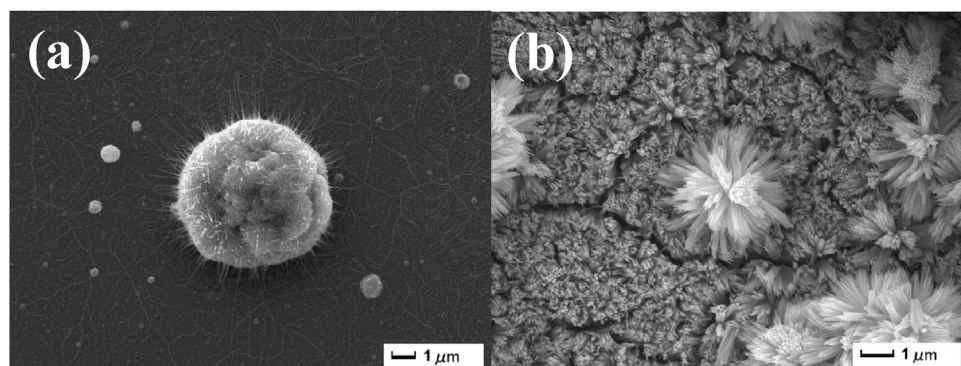


**Fig. 6.** SEM images of (a) pure Fe coating deposited by PLD and annealed at 600 °C and (b)  $Fe_2O_3$  flower-like nanostructure coating synthesized by hydrothermal method.

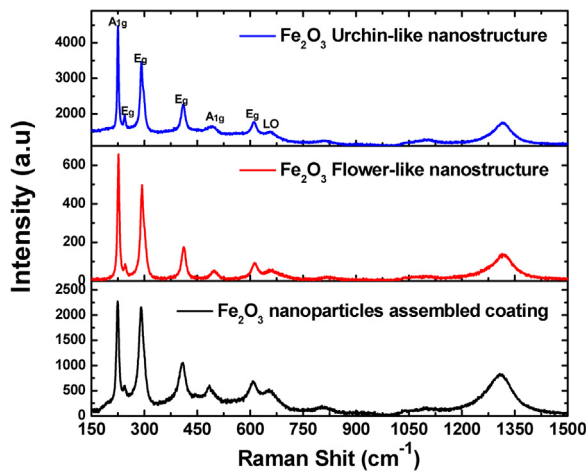


**Fig. 7.** Raman spectra of  $\text{Fe}_2\text{O}_3$  urchin-like with 1D nanostructures,  $\text{Fe}_2\text{O}_3$  flower-like with 2D nanostructure and  $\text{Fe}_2\text{O}_3$  nanoparticle assembled coating.

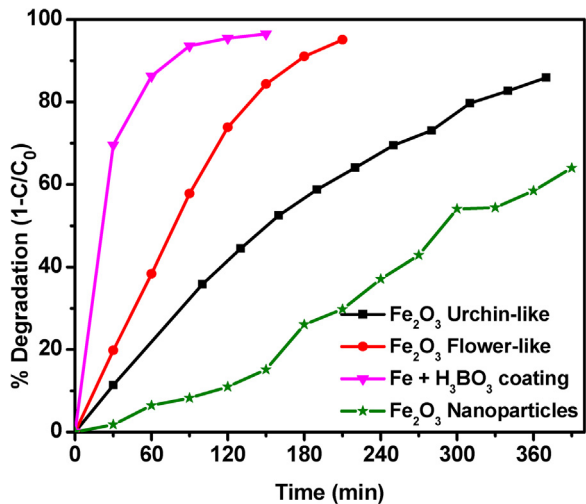


**Fig. 8.** Time dependent photocatalytic degradation ratio of MB solution in presence of  $\text{H}_2\text{O}_2$  and visible light using  $\text{Fe} + \text{H}_3\text{BO}_3$  coatings,  $\text{Fe}_2\text{O}_3$  urchin-like with 1D nanostructures,  $\text{Fe}_2\text{O}_3$  flower-like with 2D nanostructure and  $\text{Fe}_2\text{O}_3$  nanoparticle assembled coating.

by 2D nanosheets of width 200–300 nm like in case of  $\text{Fe} + \text{H}_3\text{BO}_3$  coating (Fig. 6b). Micro-Raman analysis (Fig. 7) showed that all the three coatings with different nanostructures have crystalline  $\alpha$ - $\text{Fe}_2\text{O}_3$  phase, with all the modes of vibration assigned to  $\alpha$ - $\text{Fe}_2\text{O}_3$ . The photocatalytic activity for MB dye degradation of these three coatings was compared with  $\text{Fe} + \text{H}_3\text{BO}_3$  coating annealed at 600 °C (by maintaining the catalyst weight and area of the substrate) and is reported in Fig. 8. The degradation rate increases in the following order coating A < coating B < coating C <  $\text{Fe} + \text{H}_3\text{BO}_3$  coating. NPs assembled coating with crystalline  $\alpha$ - $\text{Fe}_2\text{O}_3$  phase establish lowest photocatalytic activity while maximum degradation rate is attained with  $\text{Fe} + \text{H}_3\text{BO}_3$  coating (annealed at 600 °C) thus showing that hierarchical nanostructures with crystalline  $\alpha$ - $\text{Fe}_2\text{O}_3$  are more effective than only crystalline  $\alpha$ - $\text{Fe}_2\text{O}_3$ . Among nanostructures, the flower-like with 2D nanostructures (coating C) displays better photocatalytic activity as compared to only urchin-like nanostructures with 1D nanostructures (coating B). However, combined nanostructures of urchin-like and flower-like produced highest activity in case of  $\text{Fe} + \text{H}_3\text{BO}_3$  coatings. The above results clearly indicate that the considerably high degradation rate achieved with  $\text{Fe} + \text{H}_3\text{BO}_3$  coatings is owing to the synergic effect created by the combination of urchin-like particle with 1D NWs or NRs and flower-like parti-

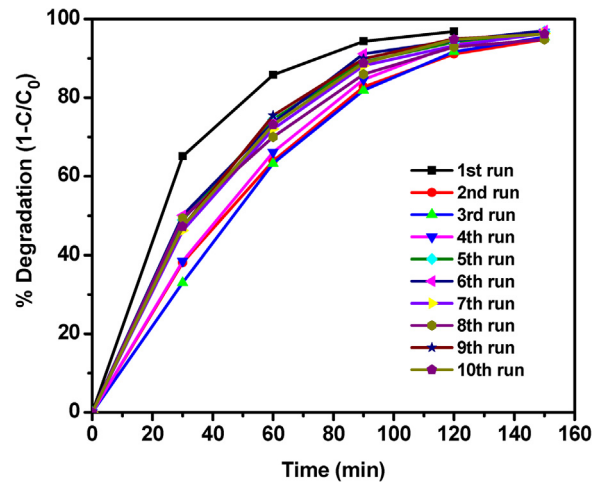


**Fig. 9.** Recycling behavior for MB dye degradation using  $\text{Fe} + \text{H}_3\text{BO}_3$  coatings synthesized by PLD and annealed in air for 4 h at 600 °C.

cle with 2D NSs blended with crystalline  $\alpha$ - $\text{Fe}_2\text{O}_3$  phase. While a mixed  $\text{Fe}_2\text{O}_3/\text{Fe}_3\text{O}_4$  phase is reported to enhance photocatalytic activity [76], in our case  $\text{Fe}_3\text{O}_4$  is not detected on the surface, but it is in the core, thus it is separated from the surface by an iron-boron oxide shell of hundreds of nanometers in thickness. While a heterojunction might indeed be found at the interface between the magnetite core and the  $\text{FeBO}_3/\text{Fe}_2\text{O}_3$  shell, it is unlikely that the resulting space charge width is large enough to influence the material surface layers involved in photocatalysis, some hundreds of nanometers away. In fact, the space charge width critically depends on the presence and density of dopants and on the charge-carriers mobility. In our case the material is un-doped and both electron and hole mobility are generally poor for iron oxides, a known problem limiting their application, for example, as photo-electrode materials [77–79]. For this reason  $\text{Fe}_3\text{O}_4$  cannot play a major role in photocatalytic enhancement in the case of  $\text{Fe} + \text{H}_3\text{BO}_3$  coatings.

### 3.3. Stability test

An important characteristic of a photocatalyst, in particular for industrial applications, is the reusability. For this reason, the recyclability of the  $\text{Fe} + \text{H}_3\text{BO}_3$  photocatalyst was tested and the results are reported in Fig. 9. After the first cycle, there is a little decrease of the activity, which remains constant during the next 9 cycles measured. This decrease in the activity is attributed to the loss of negligible amount of catalyst in the form of loose particles present on the surface of coating probably during constant stirring and washing after the first run. However, the coating is very stable with good adhesion; in fact, during the successive tests, no powder or particles were present in the solution or near the stirrer (since a magnetic stirrer was used). Importantly, even after 10-runs of recycling the MB degradation efficiencies is maintained, indicating that the 3D hierarchical nanostructure of the coating is retained without deactivation. In order to verify the stability of hierarchical nanostructures, the surface morphology and structure were investigated before and after the 10 cycles by using SEM and Raman spectroscopy respectively (Fig. 10). The urchin-like and flower-like nanostructures are well maintained after 10 cycles (inset of Fig. 10). However, in urchin structure few broken long NWs are observed which is likely due to continuous stirring during the degradation reaction. No apparent changes in the morphology suggest a very high resistance to water friction which means that it can be utilized as catalyst bed in continuous flow reactor. Micro-Raman spectra (Fig. 10) of the recycled sample confirm that the phase composition remains constant during the entire recycling tests.

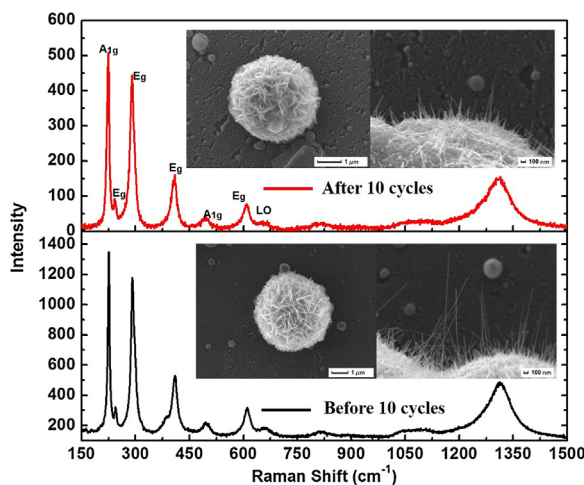


**Fig. 10.** Raman spectra of Fe-H<sub>3</sub>BO<sub>3</sub> coatings synthesized by PLD and annealed in air for 4 h at 600 °C and reused for 10 cycles. Inset shows the corresponding SEM images.

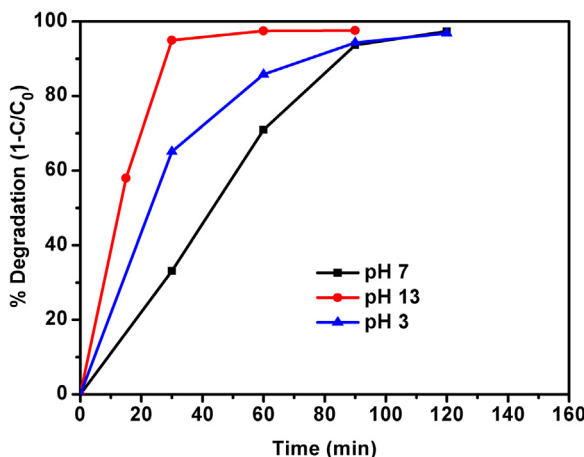


**Fig. 11.** Time dependent photocatalytic degradation ratio of MB solution in different pH conditions in presence of H<sub>2</sub>O<sub>2</sub> and visible light using Fe-H<sub>3</sub>BO<sub>3</sub> coatings.

Generally, not deionized water, but municipal tap water is used in industries which can poison the catalyst due to the presence of ionic impurities. Thus, the efficiency of the catalyst was tested in normal tap water that could be more realistic scenario and requires more robust catalyst coating. From Fig. S4, it is visible that degradation of MB dye reached up to 90% after 180 min for tap water and 97% of degradation in 120 min for DI water. But, the efficiency of the catalyst is acceptable and the marginal decrease in activity is due to the presence of dissolved ions in water.

Industrial waste waters are found in variety of pH range depending upon the type of applications, and this can affect the activity and stability of the catalyst. In order to test the robustness of our developed hierarchical nanostructures coating, a proper experiment was performed where MB degradation tests were carried out in three different pH media, namely acidic (pH 3), neutral (pH 7) and basic (pH 13). The pH of the solution was varied by adding H<sub>2</sub>SO<sub>4</sub> or KOH to realize acidic or basic pH respectively. The degradation curves (Fig. 11) show that for pH 13, the degradation reached 96% in only 30 min. In acid or neutral solution, the degradation efficiencies were almost the same: in both the cases a degradation of 96% was reached in 120 min. The only difference was the shape of the curves where the degradation rate is almost linear for pH 7. The highest activity in basic solution is not unexpected and which may be due to two main reasons: a) H<sub>2</sub>O<sub>2</sub> is acidic and its conjugate base (HOO<sup>-</sup>) is more

reactive and b) the hematite chemical stability is enhanced in basic solutions. The fact that the material is apparently stable also in the lower pH experiment, where, according to the Pourbaix diagram for the iron-water system [80], the dominant species is solvated Fe(II), might be explained by a slow kinetics of the dissolution process in absence of an applied voltage. However, the results point out that the stability of the coating is very high and by varying pH can be a simple and effective way to enhance the photo degradation of organic molecules.

#### 4. Conclusion

3D hierarchical nanostructured  $\alpha$ -Fe<sub>2</sub>O<sub>3</sub> coatings on glass substrate were prepared by pulsed laser deposition, in oxygen atmosphere, with targets made by homogeneous mixture of Fe and H<sub>3</sub>BO<sub>3</sub>. The as deposited coatings are made of metallic Fe particulates embedded in H<sub>3</sub>BO<sub>3</sub>. Subsequent thermal annealing of the as deposited coating at 600 °C, led to formation of crystalline, hierarchical 3D nanostructures made of nanowires, nanorods, and nanosheets. Stress-induced phase segregation and stress release process during thermal annealing are suggested as the growth mechanisms of these nanostructures. The synthesized nanostructures were tested for degradation of Methylene Blue dye and it was proved that degradation occurs through radicals generated by Photo-Fenton reaction.

Hematite nanostructures prepared by thermal annealing of as deposited metallic Fe coating, hematite nanoparticles assembled coating by PLD, hematite nanostructures prepared by hydrothermal chemical method were compared in photocatalytic degradation. All these coatings show lower photocatalytic activity as compared to the hematite coating obtained from thermal annealing of Fe + H<sub>3</sub>BO<sub>3</sub> sample where urchin-like and flower-like nanostructures are present. This result clearly indicates that the higher degradation rate achieved with the annealed Fe + H<sub>3</sub>BO<sub>3</sub> coatings is related to the synergic effect produced by the combination of urchin-like particle with 1D NWs or NRs and flower-like particle with 2D NSs blended with crystalline  $\alpha$ -Fe<sub>2</sub>O<sub>3</sub> phase. It is suggested that the complex surface morphology connected to the presence of several kinds of hierarchical nanostructures allows to a most efficient interaction of the catalytic surface with the reactants. Several parameters such as effect of H<sub>2</sub>O<sub>2</sub> concentration, effect of pH, water medium and recyclability tests for 10 times were finally analyzed. All tests revealed promising results in terms of enhanced activity and high mechanical stability of the 3D hierarchical nanostructures of Iron Oxides coatings.

#### Acknowledgements

The research activity is partially supported by PAT (Provincia Autonoma di Trento) project ENAM in co-operation with Istituto PCB of CNR (Italy). R. Fernandes, K. Datte and N. Patel acknowledges UGC for providing financial support through Dr. D.S. Kothari postdoctoral fellowship program and Faculty recharge program respectively. We gratefully acknowledge Claudio Cestari for technical help and Dr. Cristina Armellini for X-ray diffraction measurements. We acknowledge Martina Azzolini for preliminary measurements.

#### Appendix A. Supplementary data

Supplementary data associated with this article can be found, in the online version, at <http://dx.doi.org/10.1016/j.apcatb.2017.07.063>.

## References

[1] Q. Zhang, Y. Huang, S. Peng, Y. Zhang, Z. Shen, J.-j. Cao, W. Ho, S.C. Lee, D.Y.H. Pui, Perovskite LaFeO<sub>3</sub>-SrTiO<sub>3</sub> composite for synergistically enhanced NO removal under visible light excitation, *Appl. Catal. B: Environ.* 204 (2017) 346–357.

[2] Z. Wang, Y. Huang, W. Ho, J. Cao, Z. Shen, S.C. Lee, Fabrication of Bi<sub>2</sub>O<sub>2</sub>CO<sub>3</sub>/g-C<sub>3</sub>N<sub>4</sub> heterojunctions for efficiently photocatalytic NO in air removal: in-situ self-sacrificial synthesis, characterizations and mechanistic study, *Appl. Catal. B: Environ.* 199 (2016) 123–133.

[3] Q. Zhang, Y. Huang, L. Xu, J.-j. Cao, W. Ho, S.C. Lee, Visible-light-active plasmonic Ag-SrTiO<sub>3</sub> nanocomposites for the degradation of NO in air with high selectivity, *ACS Appl. Mater. Interfaces* 8 (2016) 4165–4174.

[4] P. Liu, C. Li, Z. Zhao, G. Lu, H. Cui, W. Zhang, Induced effects of advanced oxidation processes, *Sci. Rep.* 4 (2014) 4018.

[5] M.A. Shannon, P.W. Bohn, M. Elimelech, J.G. Georgiadis, B.J. Marinas, A.M. Mayes, Science and technology for water purification in the coming decades, *Nature* 452 (2008) 301–310.

[6] C. von Sonntag, Advanced oxidation processes: mechanistic aspects, *Water Sci. Technol.* 58 (2008) 1015–1021.

[7] S. Guo, G. Zhang, J. Wang, Photo-Fenton degradation of rhodamine B using Fe<sub>2</sub>O<sub>3</sub>-Kaolin as heterogeneous catalyst: characterization, process optimization and mechanism, *J. Colloid Interface Sci.* 433 (2014) 1–8.

[8] S. Malato, P. Fernández-Ibáñez, M.I. Maldonado, J. Blanco, W. Gernjak, Decontamination and disinfection of water by solar photocatalysis: recent overview and trends, *Catal. Today* 147 (2009) 1–59.

[9] C.-C. Kuan, S.-Y. Chang, S.L.M. Schroeder, Fenton-like oxidation of 4-chlorophenol: homogeneous or heterogeneous? *Ind. Eng. Chem. Res.* 54 (2015) 8122–8129.

[10] P.C.K. Vensborg, T.F. Jaramillo, Addressing the terawatt challenge: scalability in the supply of chemical elements for renewable energy, *RSC Adv.* 2 (2012) 7933–7947.

[11] M.V. Reddy, T. Yu, C.H. Sow, Z.X. Shen, C.T. Lim, G.V. Subba Rao, B.V.R. Chowdari,  $\alpha$ -Fe<sub>2</sub>O<sub>3</sub> nanoflakes as an anode material for Li-ion batteries, *Adv. Funct. Mater.* 17 (2007) 2792–2799.

[12] H.T. Tan, W. Sun, L. Wang, Q. Yan, 2D transition metal oxides/hydroxides for energy-storage applications, *ChemNanoMat* 2 (2016) 562–577.

[13] M. Chen, E. Zhao, Q. Yan, Z. Hu, X. Xiao, D. Chen, The effect of crystal face of Fe<sub>2</sub>O<sub>3</sub> on the electrochemical performance for lithium-ion batteries, *Sci. Rep.* 6 (2016) 29381.

[14] L. Zhang, H.B. Wu, X.W. Lou, Iron-oxide-based advanced anode materials for lithium-ion batteries, *Adv. Energy Mater.* 4 (2014).

[15] B. Wang, J.S. Chen, X.W. Lou, The comparative lithium storage properties of urchin-like hematite spheres: hollow vs. solid, *J. Mater. Chem.* 22 (2012) 9466–9468.

[16] L.-C. Hsu, H.-C. Yu, T.-H. Chang, Y.-Y. Li, Formation of three-dimensional urchin-like  $\alpha$ -Fe<sub>2</sub>O<sub>3</sub> structure and its field-emission application, *ACS Appl. Mater. Interfaces* 3 (2011) 3084–3090.

[17] Y. Zhang, Y. Jia, A facile precursor calcination approach to iron oxide micro/nanostructures with a high magnetization, *J. Alloys Compd.* 659 (2016) 66–73.

[18] C. Zhu, C. Li, M. Zheng, J.-J. Delaunay, Plasma-induced oxygen vacancies in ultrathin hematite nanoflakes promoting photoelectrochemical water oxidation, *ACS Appl. Mater. Interfaces* 7 (2015) 22355–22363.

[19] Y. Qiu, S.-F. Leung, Q. Zhang, B. Hua, Q. Lin, Z. Wei, K.-H. Tsui, Y. Zhang, S. Yang, Z. Fan, Efficient photoelectrochemical water splitting with ultrathin films of hematite on three-dimensional nanophotonic structures, *Nano Lett.* 14 (2014) 2123–2129.

[20] J.-W. Jang, C. Du, Y. Ye, Y. Lin, X. Yao, J. Thorne, E. Liu, G. McMahon, J. Zhu, A. Javey, J. Guo, D. Wang, Enabling unassisted solar water splitting by iron oxide and silicon, *Nat. Commun.* 6 (2015).

[21] N. Dalle Carbonare, S. Carli, R. Argazzi, M. Orlandi, N. Bazzanella, A. Miotello, S. Caramori, C.A. Bignozzi, Improvement of the electron collection efficiency in porous hematite using a thin iron oxide underlayer: towards efficient all-iron based photoelectrodes, *Phys. Chem. Chem. Phys.* 17 (2015) 29661–29670.

[22] M. Orlandi, N. Dalle Carbonare, S. Caramori, C.A. Bignozzi, S. Berardi, A. Mazzi, Z. El Koura, N. Bazzanella, N. Patel, A. Miotello, Porous versus compact nanosized Fe(III)-based water oxidation catalyst for photoanodes functionalization, *ACS Appl. Mater. Interfaces* 8 (2016) 20003–20011.

[23] Z.-F. Dou, C.-Y. Cao, Q. Wang, J. Qu, Y. Yu, W.-G. Song, Synthesis, self-assembly, and high performance in gas sensing of X-shaped iron oxide crystals, *ACS Appl. Mater. Interfaces* 4 (2012) 5698–5703.

[24] J.-H. Lee, Gas sensors using hierarchical and hollow oxide nanostructures: overview, *Sens. Actuators B: Chem.* 140 (2009) 319–336.

[25] P. Sun, L. You, D. Wang, Y. Sun, J. Ma, G. Lu, Synthesis and gas sensing properties of bundle-like  $\alpha$ -Fe2O3 nanorods, *Sens. Actuators B: Chem.* 156 (2011) 368–374.

[26] F. Zhang, H. Yang, X. Xie, L. Li, L. Zhang, J. Yu, H. Zhao, B. Liu, Controlled synthesis and gas-sensing properties of hollow sea urchin-like  $\alpha$ -Fe<sub>2</sub>O<sub>3</sub> nanostructures and  $\alpha$ -Fe<sub>2</sub>O<sub>3</sub> nanocubes, *Sens. Actuators B: Chem.* 141 (2009) 381–389.

[27] D. Ling, T. Hyeon, Chemical design of biocompatible iron oxide nanoparticles for medical applications, *Small* 9 (2013) 1450–1466.

[28] F. Ai, C.A. Ferreira, F. Chen, W. Cai, Engineering of radiolabeled iron oxide nanoparticles for dual-modality imaging, *Wiley Interdiscip. Rev.: Nanomed. Nanobiotechnol.* 8 (2016) 619–630.

[29] X. Li, J. Yu, M. Jaroniec, Hierarchical photocatalysts, *Chem. Soc. Rev.* 45 (2016) 2603–2636.

[30] L.S. Zhong, J.S. Hu, H.P. Liang, A.M. Cao, W.G. Song, L.J. Wan, Self-assembled 3D flowerlike iron oxide nanostructures and their application in water treatment, *Adv. Mater.* 18 (2006) 2426–2431.

[31] A. Yürüm, Z.Ö. Kocabas-Ataklı, M. Sezen, R. Semiat, Y. Yürüm, Fast deposition of porous iron oxide on activated carbon by microwave heating and arsenic (V) removal from water, *Chem. Eng. J.* 242 (2014) 321–332.

[32] F.N. Sayed, V. Polshettiwar, Facile and sustainable synthesis of shaped iron oxide nanoparticles: effect of iron precursor salts on the shapes of iron oxides, *Sci. Rep.* 5 (2015) 9733.

[33] H.U. Lee, S.C. Lee, Y.-C. Lee, S. Vrtnik, C. Kim, S. Lee, Y.B. Lee, B. Nam, J.W. Lee, S.Y. Park, S.M. Lee, J. Lee, Sea-urchin-like iron oxide nanostructures for water treatment, *J. Hazard. Mater.* 262 (2013) 130–136.

[34] X. Qu, N. Kobayashi, T. Komatsu, Solid nanotubes comprising  $\alpha$ -Fe<sub>2</sub>O<sub>3</sub> nanoparticles prepared from ferritin protein, *ACS Nano* 4 (2010) 1732–1738.

[35] L. Demarchis, M. Minella, R. Nisticò, V. Maurino, C. Minero, D. Vione, Photo-Fenton reaction in the presence of morphologically controlled hematite as iron source, *J. Photochem. Photobiol. A: Chem.* 307–308 (2017) 99–107.

[36] H. Lan, A. Wang, R. Liu, H. Liu, J. Qu, Heterogeneous photo-Fenton degradation of acid red B over Fe2O3 supported on activated carbon fiber, *J. Hazard. Mater.* 285 (2015) 167–172.

[37] J.Y.T. Chan, S.Y. Ang, E.Y. Ye, M. Sullivan, J. Zhang, M. Lin, Heterogeneous photo-Fenton reaction on hematite ([small alpha]-Fe2O3){104}, {113} and {001} surface facets, *Phys. Chem. Chem. Phys.* 17 (2015) 25333–25341.

[38] Y. Jiao, Y. Liu, F. Qu, A. Umar, X. Wu, Visible-light-driven photocatalytic properties of simply synthesized  $\alpha$ -Iron(III)oxide nanourchins, *J. Colloid Interface Sci.* 451 (2015) 93–100.

[39] S. Zhang, J. Li, H. Niu, W. Xu, J. Xu, W. Hu, X. Wang, Visible-light photocatalytic degradation of methylene blue using SnO<sub>2</sub>/ $\alpha$ -Fe2O3 hierarchical nanostructures, *ChemPlusChem* 78 (2013) 192–199.

[40] M.A. Ahmed, E.E. El-Katori, Z.H. Gharni, Photocatalytic degradation of methylene blue dye using Fe<sub>2</sub>O<sub>3</sub>/TiO<sub>2</sub> nanoparticles prepared by sol-gel method, *J. Alloys Compd.* 553 (2013) 19–29.

[41] S. Yun, Y.-C. Lee, H.S. Park, Phase-controlled iron oxide nanobox deposited on hierarchically structured graphene networks for lithium ion storage and photocatalysis, *Sci. Rep.* 6 (2016) 19959.

[42] S. Lin, L. Liu, J. Hu, Y. Liang, W. Cui, Nano Ag@AgBr surface-sensitized Bi<sub>2</sub>WO<sub>6</sub> photocatalyst: oil-in-water synthesis and enhanced photocatalytic degradation, *Appl. Surf. Sci.* 324 (2015) 20–29.

[43] J. Hu, W. An, H. Wang, J. Geng, W. Cui, Y. Zhan, Synthesis of a hierarchical BiOBr nanodots/Bi<sub>2</sub>WO<sub>6</sub> p-n heterostructure with enhanced photoinduced electric and photocatalytic degradation performance, *RSC Adv.* 6 (2016) 29554–29562.

[44] X.S. Nguyen, G. Zhang, X. Yang, Mesocrystalline Zn-doped Fe<sub>3</sub>O<sub>4</sub> hollow submicropores: formation mechanism and enhanced photo-Fenton catalytic performance, *ACS Appl. Mater. Interfaces* 9 (2017) 8900–8909.

[45] Y. Gao, H. Gan, G. Zhang, Y. Guo, Visible light assisted Fenton-like degradation of rhodamine B and 4-nitrophenol solutions with a stable poly-hydroxyl-iron/sepiolite catalyst, *Chem. Eng. J.* 217 (2013) 221–230.

[46] S. Guo, N. Yuan, G. Zhang, J.C. Yu, Graphene modified iron sludge derived from homogeneous Fenton process as an efficient heterogeneous Fenton catalyst for degradation of organic pollutants, *Microporous Mesoporous Mater.* 238 (2017) 62–68.

[47] N.A. Zubir, C. Yacou, J. Motuzas, X. Zhang, J.C. Diniz da Costa, Structural and functional investigation of graphene oxide-Fe<sub>3</sub>O<sub>4</sub> nanocomposites for the heterogeneous Fenton-like reaction, *Sci. Rep.* 4 (2014) 4594.

[48] H. Park, Y.-C. Lee, B.G. Choi, Y.S. Choi, J.-W. Yang, W.H. Hong, Energy transfer in ionic-liquid-functionalized inorganic nanorods for highly efficient photocatalytic applications, *Small* 6 (2010) 290–295.

[49] T. Warang, N. Patel, R. Fernandes, N. Bazzanella, A. Miotello, Co<sub>3</sub>O<sub>4</sub> nanoparticles assembled coatings synthesized by different techniques for photo-degradation of methylene blue dye, *Appl. Catal. B: Environ.* 132–133 (2013) 204–211.

[50] N. Patel, T. Warang, R. Fernandes, C. Cestari, D. Avi, N. Bazzanella, R. Edla, Z.E. Koura, A. Miotello, A new apparatus for carbon monoxide oxidation studies performed over thin film catalysts, *Meas. Sci. Technol.* 24 (2013) 125901.

[51] R. Edla, N. Patel, Z. El Koura, R. Fernandes, N. Bazzanella, A. Miotello, Pulsed laser deposition of Co<sub>3</sub>O<sub>4</sub> nanocatalysts for dye degradation and CO oxidation, *Appl. Surf. Sci.* 302 (2014) 105–108.

[52] R. Edla, S. Gupta, N. Patel, N. Bazzanella, R. Fernandes, D.C. Kothari, A. Miotello, Enhanced H<sub>2</sub> production from hydrolysis of sodium borohydride using Co<sub>3</sub>O<sub>4</sub> nanoparticles assembled coatings prepared by pulsed laser deposition, *Appl. Catal. A: Gen.* 515 (2016) 1–9.

[53] R. Edla, N. Patel, M. Orlandi, N. Bazzanella, V. Bello, C. Maurizio, G. Mattei, P. Mazzoldi, A. Miotello, Highly photo-catalytically active hierarchical 3D porous/urchin nanostructured Co<sub>3</sub>O<sub>4</sub> coating synthesized by Pulsed Laser Deposition, *Appl. Catal. B: Environ.* 166–167 (2015) 475–484.

[54] F. Švegl, B. Orel, I. Grabec-Švegl, V. Kaučič, Characterization of spinel Co<sub>3</sub>O<sub>4</sub> and Li-doped Co<sub>3</sub>O<sub>4</sub> thin film electrocatalysts prepared by the sol-gel route, *Electrochim. Acta* 45 (2000) 4359–4371.

[55] M.A. Mahadik, S.S. Shinde, K.Y. Rajpure, C.H. Bhosale, Photocatalytic oxidation of Rhodamine B with ferric oxide thin films under solar illumination, *Mater. Res. Bull.* 48 (2013) 4058–4065.

[56] M.A. Mahadik, S.S. Shinde, S.S. Kumbhar, H.M. Pathan, K.Y. Rajpure, C.H. Bhosale, Enhanced photocatalytic activity of sprayed Au doped ferric oxide thin films for salicylic acid degradation in aqueous medium, *J. Photochem. Photobiol. B: Biol.* 142 (2015) 43–50.

[57] J. Wöllenstein, M. Burgmair, G. Plescher, T. Sulima, J. Hildenbrand, H. Böttner, I. Eisele, Cobalt oxide based gas sensors on silicon substrate for operation at low temperatures, *Sens. Actuators B: Chem.* 93 (2003) 442–448.

[58] S.C. Singh, H. Zeng, Nanomaterials and nanopatterns based on laser processing: a brief review on current state of art, *Sci. Adv. Mater.* 4 (2012) 368–390.

[59] A. Miotello, N. Patel, Pulsed laser deposition of cluster-assembled films for catalysis and the photocatalysis relevant to energy and the environment, *Appl. Surf. Sci.* 278 (2013) 19–25.

[60] P. Sun, W. Wang, Y. Liu, Y. Sun, J. Ma, G. Lu, Hydrothermal synthesis of 3D urchin-like  $\alpha$ -Fe<sub>2</sub>O<sub>3</sub> nanostructure for gas sensor, *Sens. Actuators B: Chem.* 173 (2012) 52–57.

[61] J. Kim, M.K. Chung, B.H. Ka, J.H. Ku, S. Park, J. Ryu, S.M. Oh, The role of metallic Fe and carbon matrix in Fe<sub>2</sub>O<sub>3</sub> / Fe / carbon nanocomposite for lithium-ion batteries, *J. Electrochem. Soc.* 157 (2010) A412–A417.

[62] G. Tong, W. Wu, J. Guan, H. Qian, J. Yuan, W. Li, Synthesis and characterization of nanosized urchin-like  $\alpha$ -Fe<sub>2</sub>O<sub>3</sub> and Fe<sub>3</sub>O<sub>4</sub>: microwave electromagnetic and absorbing properties, *J. Alloys Compd.* 509 (2011) 4320–4326.

[63] A. Atasoy, The aluminothermic reduction of boric acid, *Int. J. Refract. Met. Hard Mater.* 28 (2010) 616–622.

[64] A.M. Jubb, H.C. Allen, Vibrational spectroscopic characterization of hematite, maghemite, and magnetite thin films produced by vapor deposition, *ACS Appl. Mater. Interfaces* 2 (2010) 2804–2812.

[65] F.L. Galeener, G. Lucovsky, J.C. Mikkelsen, Vibrational spectra and the structure of pure vitreous B2O3, *Phys. Rev. B* 22 (1980) 3983–3990.

[66] R. Arenal, A.C. Ferrari, S. Reich, L. Wirtz, J.Y. Mevellec, S. Lefrant, A. Rubio, A. Loiseau, Raman spectroscopy of single-wall boron nitride nanotubes, *Nano Lett.* 6 (2006) 1812–1816.

[67] I.W. Shepherd, Raman scattering in FeBO<sub>3</sub>, *J. Appl. Phys.* 42 (1971) 1482–1483.

[68] Y. El Mendili, J.-F. Bardeau, N. Randrianantoandro, F. Grasset, J.-M. Grenache, Insights into the mechanism related to the phase transition from  $\gamma$ -Fe<sub>2</sub>O<sub>3</sub> to  $\alpha$ -Fe<sub>2</sub>O<sub>3</sub> nanoparticles induced by thermal treatment and laser irradiation, *J. Phys. Chem. C* 116 (2012) 23785–23792.

[69] A.P. Grosvenor, B.A. Kobe, M.C. Biesinger, N.S. McIntyre, Investigation of multiplet splitting of Fe 2p XPS spectra and bonding in iron compounds, *Surf. Interface Anal.* 36 (2004) 1564–1574.

[70] V.V. Atuchin, D.A. Vinnik, T.A. Gavrilova, S.A. Gudkova, L.I. Isaenko, X. Jiang, L.D. Pokrovsky, I.P. Prosvirin, L.S. Mashkovtseva, Z. Lin, Flux crystal growth and the electronic structure of BaFe12O19 hexaferrite, *J. Phys. Chem. C* 120 (2016) 5114–5123.

[71] P.P. Craig, V. Radeka, Stress dependence of contact potential: the ac Kelvin method, *Rev. Sci. Instrum.* 41 (1970) 258–264.

[72] D. Kramer, Dependence of surface stress, surface energy and surface tension on potential and charge, *Phys. Chem. Chem. Phys.* 10 (2008) 168–177.

[73] A. Miotello, R. Kelly, Laser-induced phase explosion: new physical problems when a condensed phase approaches the thermodynamic critical temperature, *Appl. Phys. A* 69 (1999) S67–S73.

[74] N. Patel, G. Guella, A. Kale, A. Miotello, B. Patton, C. Zanchetta, L. Mirenghi, P. Rotolo, Thin films of Co-B prepared by pulsed laser deposition as efficient catalysts in hydrogen producing reactions, *Appl. Catal. A: Gen.* 323 (2007) 18–24.

[75] M. Orlandi, S. Caramori, F. Ronconi, C.A. Bignozzi, Z. El Koura, N. Bazzanella, L. Meda, A. Miotello, Pulsed-laser deposition of nanostructured iron oxide catalysts for efficient water oxidation, *ACS Appl. Mater. Interfaces* 6 (2014) 6186–6190.

[76] R.C.C. Costa, M.F.F. Lelis, L.C.A. Oliveira, J.D. Fabris, J.D. Ardisson, R.R.V.A. Rios, C.N. Silva, R.M. Lago, Novel active heterogeneous Fenton system based on Fe<sub>3</sub>-xMxO<sub>4</sub> (Fe, Co, Mn, Ni): the role of M<sup>2+</sup> species on the reactivity towards H<sub>2</sub>O<sub>2</sub> reactions, *J. Hazard. Mater.* 129 (2006) 171–178.

[77] A.J. Bosman, H.J. van Daal, Small-polaron versus band conduction in some transition-metal oxides, *Adv. Phys.* 19 (1970) 1–117.

[78] S. Onari, T. Arai, K. Kudo, Infrared lattice vibrations and dielectric dispersion in  $\alpha$ -Fe<sub>2</sub>O<sub>3</sub>, *Phys. Rev. B* 16 (1977) 1717–1721.

[79] K.M. Rosso, D.M.A. Smith, M. Dupuis, An ab initio model of electron transport in hematite ( $\alpha$ -Fe<sub>2</sub>O<sub>3</sub>) basal planes, *J. Chem. Phys.* 118 (2003) 6455–6466.

[80] D.E.J. Talbot, J.D.R. Talbot, *Corrosion Science and Technology*, CRC Press, 2010.